Wave–ice interactions in the marginal ice zone. Part 2: Numerical implementation and sensitivity studies along 1D transects of the ocean surface

Timothy D. Williams [a,*], Luke G. Bennetts [b], Vernon A. Squire [c], Dany Dumont [d], Laurent Bertino [a,e]

[a] Nansen Environmental and Remote Sensing Center, Thormøhlensgate 47, 5006 Bergen, Norway
[b] School of Mathematical Sciences, North Terrace Campus, The University of Adelaide, SA 5005, Australia
[c] Department of Mathematics and Statistics, University of Otago, P.O. Box 56, Dunedin 9054, New Zealand
[d] Institut des sciences de la mer de Rimouski, 310 alle des Ursulines, C.P. 3300, Rimouski, Québec G5L 3A1, Canada
[e] Bjerknes Center for Climate Research, Bergen, Norway

ABSTRACT

The theoretical foundation of a wave–ice interaction model is reported in Part 1 of this study. The model incorporates attenuation of ocean surface waves by sea ice floes and the concomitant breaking of the floes by waves that determines the structure of the marginal ice zone (MIZ). A numerical implementation of the method is presented here. Convergence of the numerical method is demonstrated, as temporal and spatial grids are refined. A semi-analytical method, which does not require time-stepping, is also developed to validate the numerical results, when dispersion is neglected. The wave energy lost during ice breakage is parameterized, as part of the numerical method. Sensitivity studies are conducted in relation to the energy loss and also dispersive effects, the choice of the attenuation model, the properties of the wave field, and sea ice properties such as concentration, thickness and breaking strain. Example simulations intended to represent conditions in the Fram Strait in 2007, which exploit reanalyzed wave and ice model data, are shown to conclude the results section. These are compared to estimates of MIZ widths based on a concentration criteria, and obtained from remotely-sensed passive microwave images.

© 2013 Elsevier Ltd. All rights reserved.

1. Introduction

Predictions of wave and ice conditions in the marginal ice zone (MIZ) are becoming increasingly important in the era of climate change and enhanced access to the Arctic Ocean. However, contemporary sea ice models do not contain information on floe sizes, and contemporary wave models generally do not extend into the ice-covered ocean. Modeling the interactions of ocean surface waves with sea ice is necessary to rectify these conspicuous omissions, because (i) floe sizes in the MIZ are far smaller than those in the ice interior due to wave-induced ice breakage (Toyota et al., 2006), and (ii) the presence of the ice-cover strongly attenuates the waves (Wadhams et al., 1988), acting as a low-pass filter, and hence is a necessary additional consideration when modeling the transport of wave energy in the MIZ.

Part 1 of this investigation (Williams et al., 2013) describes a waves-in-ice model (WIM) that extends the work of Dumont et al. (2011) (hereafter referred to as DKB). The WIM provides predictions of (i) the ice floe size distribution (FSD) resulting from wave-induced flexural breakage of the ice cover, and (ii) the wave spectrum within the ice cover. The model includes two interrelated sub-components. First, a wave attenuation model that calculates the proportion of wave energy that is reflected by floe edges, and lost to dissipative processes, as a function of the number of ice floes encountered along the propagation path. Second, an ice breakage model that decides when the strain imposed by the passing waves on the ice cover is sufficient to cause fracture and how the resulting FSD evolves.

The FSD provided by the WIM will allow floe-size-dependent processes to be modeled in the MIZ. The smaller floe sizes in the MIZ are potentially important for thermodynamic exchanges such as lateral melting between the atmosphere, ice and ocean; dynamic exchanges, e.g., form and skin drag coefficients; and rheology, i.e., how horizontal stresses relate to deformation rates. Floe-size-dependent thermodynamic and dynamic models have been developed (e.g., Shen et al., 1986; Steele et al., 1989; Feltham, 2005), but can only be tested in fully coupled models once a floe size parameter is incorporated in sea ice models.

In this paper, we place the model theory of Part 1 into a discrete spatial and temporal framework for the purpose of numerical

* Corresponding author. Tel.: +47 46548931.
E-mail addresses: timothy.williams@nersc.no (T.D. Williams), luke.bennetts@adelaide.edu.au (L.G. Bennetts), vernon.squire@otago.ac.nz (V.A. Squire), dany_dumont@uqar.ca (D. Dumont), laurent.bertino@nersc.no (L. Bertino).

calculations. As part of the numerical scheme, we propose a method to simulate the wave energy lost during ice breakage. Semi-analytical schemes are devised for two limiting cases of wave energy loss. These two schemes neglect dispersion, which is shown to have a negligible affect on the FSD.

Here, we consider one-dimensional transects of the ocean surface only, although the full numerical algorithm can be generalized to two-dimensional ocean surfaces. The one-dimensional restriction, however, provides a convenient setting to test the sensitivities of the WIM to the key numerical and physical parameters. Idealized incident wave and ice conditions are used to investigate the influence of the grid size, time step, the wave damping parameter, wave energy lost during ice breakage and breaking strain on the FSD produced by the WIM. Numerical experiments are also conducted with 'realistic' input data that represent the Fram Strait in 2007. In the absence of measured FSD data to validate the WIM, we compare our MIZ width predictions, i.e., the length of the interval of ice cover broken by waves, with MIZ widths based on a concentration criteria, using AMSR-E satellite data.

2. Statement of the problem

We consider a one-dimensional transect $x \in [0, X_2]$ of spatially varying ice concentration $c(x)$ and thickness $h(x)$. We typically use $X_2 = 450$ km. The transect is discretized into N_x grid cells with uniform widths $\Delta x = X_2/N_x$. The ice edge is located at $x = X_1$ such that the open water region is $[0, X_1]$ and the ice-covered region is $[X_1, X_2]$ (see Fig. 1). In our idealized simulations, we use an exponential thickness profile of the form

$$h(x) = \begin{cases} 0 & \text{for } 0 < x < X_1, \\ h_\infty\big(0.1 + 0.9\big(1 - e^{-(x-X_1/X_h)}\big)\big) & \text{for } X_1 < x < X_2, \end{cases} \quad (1a)$$

and a uniform concentration

$$c(x) = \begin{cases} 0 & \text{for } 0 < x < X_1, \\ c_\infty & \text{for } X_1 < x < X_2. \end{cases} \quad (1b)$$

For realistic simulations, the concentration and thickness profiles are taken from the TOPAZ operational forecasting system (Sakov et al., 2012). The parameter X_h in (1a) was chosen to be 60 km to approximate TOPAZ thickness outputs. Table 1 lists the default values of all parameters.

The wave energy is described by the spectral density function $S(\omega; x, t)$, where $\omega = 2\pi/T$ is the angular frequency and T is the wave period. The wave spectrum is defined in both the open ocean and the ice-covered ocean, after having undergone some attenuation. The incident wave spectrum is prescribed at $x = 0$. Because data obtained from operational wave models are usually given
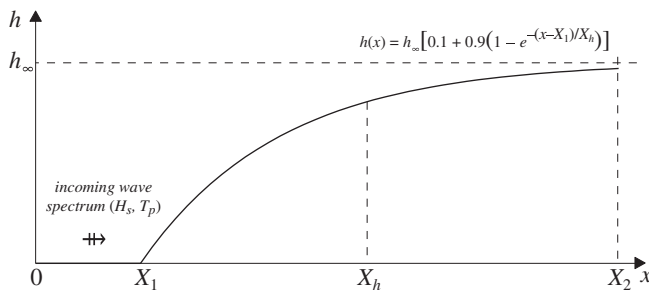
Table 1
Default model parameters.

Quantity	Symbol	Value
Ice thickness	h_∞	1–4 m
Ice concentration	c_∞	0.75
Water density	ρ	1025 kg m^{-3}
Ice density	ρ_{ice}	922.5 kg m^{-3}
Gravitational acceleration	g	9.81 m s^{-2}
Brine volume fraction	v_b	0.1
Incident significant wave height	H_s	3 m
Incident peak period	T_p	6–10 s
Minimum floe size in FSD	$D_{\min}$	20 m
FSD cut-off length	D_{unif}	200 m
Initial value of $D_{\max}$	D_{init}	500 m
Fragility	Π	0.9
Number of broken pieces	ξ	2
Number of spatial grid cells	N_x	91
Grid size	Δx	5 km
Time step	Δt	400 s
Number of spectral components	N_ω	31
Minimum wave period	$T_{30} = 2\pi/\omega_{30}$	2.5 s
Maximum wave period	$T_0 = 2\pi/\omega_0$	23.8 s
Spectral resolution	$\Delta\omega$	7.5×10^{-2} s^{-1}
Breaking probability threshold	$\mathbb{P}_c$	e$^{-1} \approx 0.37$
Flexural strength	σ_c	0.27 GPa
Effective Young's modulus	Y^*	5.5 GPa
Breaking strain	ε_c	4.99×10^{-5}
Breaking significant strain	$E_c = \varepsilon_c\sqrt{2}$	7.05×10^{-5}
Viscous damping parameter	Γ	13.0 Pa s m^{-1}

parametrically in terms of the significant wave height H_s and the peak period T_p (Ochi, 1998; WMO, 1998), we use the Bretschneider two-parameter spectrum (Bretschneider, 1959), i.e.,

$$S(\omega; 0, t) = S_B(\omega; T_p, H_s) = \frac{1.25 H_s^2 T^5}{8\pi T_p^4} e^{-1.25(T/T_p)^4}. \quad (2)$$

Note that in the realistic experiments H_s and T_p evolve in time causing the incident wave spectrum to be temporally dependent. It may be possible to obtain more detailed incident wave spectra in the future—for example spectra with a parameterization of swell as well as wind waves, or the full frequency and directional spectrum.

The FSD is characterized by two spatially varying floe length parameters $D_{\max}(x, t)$ and $\langle D \rangle(x, t)$, the maximum floe length and average floe length, respectively, which also evolve with time. The detailed parameterization of the FSD is presented in Section 4.1 of Part 1.

3. Theoretical preliminaries

In this section we recap key definitions and ideas from Part 1.

3.1. Wave statistics

Let the displacement of the (horizontal) air-ice interface be $\eta_{\text{ice}}(x, t)$. Assuming the ice can be represented by a thin plate model, the horizontal strain in the plane of the wave is

$$\varepsilon = \frac{h}{2}\partial_x^2\eta_{\text{ice}}, \quad (3)$$

where h is the ice thickness. The main statistics we are interested in are the mean square values of these quantities, $\langle\eta_{\text{ice}}^2\rangle$ and $\langle\varepsilon^2\rangle$. These give us the significant wave height H_s and the significant strain E_s:

$$H_s = 4\langle\eta_{\text{ice}}^2\rangle^{1/2}, \quad E_s = 2\langle\varepsilon^2\rangle^{1/2}. \quad (4)$$

The dominant wave period T_W also plays a role as it defines a dominant wavelength λ_W that, if breaking occurs, determines the maximum lengths of the consequent broken floes. It, like $\langle\eta_{\text{ice}}^2\rangle$ and $\langle\varepsilon^2\rangle$,

Fig. 1. Schematic figure illustrating the ice thickness profile in relation to the incident wave field. We assume the latter is prescribed at $x = 0$ using a Bretschneider spectrum of the form (2), parameterized in terms of the significant wave height H_s and peak period T_p. The thickness and concentration are either given by (1) or are taken from TOPAZ model outputs.

In the figure: $h(x) = h_\infty\big[0.1 + 0.9\big(1 - e^{-(x-X_1)/X_h}\big)\big]$; incoming wave spectrum (H_s, T_p); axes labeled h, h_∞, 0, X_1, X_h, X_2, x.

is defined in terms of integrals involving the wave spectrum S (see equations 5 and 12 of Part 1).

As discussed in Appendix A of Part 1, we assume the displacement due to a wave with the single frequency ω follows a sinusoidal profile

$$\eta_{ice}(x,t) = \text{Re}[A_{ice}e^{i(\kappa x - \omega t)}], \tag{5}$$

where $\kappa(\omega, \Gamma)$ satisfies the dispersion relation for ice-covered water, as follows

$$(F\kappa^4 + \rho(g - d\omega^2) - i\omega\Gamma)\kappa = \rho\omega^2. \tag{6}$$

In (6) F is the flexural rigidity of the ice, ρ_{ice} is the ice density, h is the ice thickness, Γ is the damping coefficient and P is the water pressure. The parameter Γ contributes to a drag pressure $(-\Gamma\partial_t\eta_{ice})$ that is proportional to the particle velocity and which is usually absent from the thin plate formulation. The rigidity is given by $F = Y^*h^3/12(1 - v^2)$, where Y^* is the effective Young's Modulus and $v = 0.3$ is the Poisson's ratio.

Let $k_{ice}(\omega) = K(\omega, 0)$ be the real positive root of (6) when $\Gamma = 0$. When $\Gamma > 0$, this root becomes complex, and $\kappa \approx k_{ice}(\omega) + i\delta(\omega, \Gamma)$, where $\delta > 0$ is small enough to be ignored on small-scale computations, and only makes a significant contribution to large scale wave attenuation. Also let

$$W(\omega) = \frac{gk_{ice}}{\omega^2}|\mathcal{T}|, \quad E(\omega) = \frac{h}{2}k_{ice}^2 W(\omega); \tag{7}$$

W is a factor that approximately converts the wave amplitude in open water, A, to the wave amplitude in ice, i.e., $A_{ice} \approx WA$, and $\mathcal{T}$ is the transmission coefficient for a wave traveling from a region of open water into an ice-covered region (Williams and Porter, 2009), which depends on both ω and the ice properties involved in (6). Similarly the strain amplitude is $E_W \approx EA$.

We now define the following integrals over frequency:

$$m_n[\eta_{ice}] = \int_0^\infty S(\omega)\omega^n W^2(\omega)d\omega, \tag{8a}$$

$$m_n[\varepsilon] = \int_0^\infty S(\omega)\omega^n E^2(\omega)d\omega. \tag{8b}$$

These integrals can be used to determine the expected response to a given wave field in a way that allows for the possibility of constructive and destructive interference between frequencies. Our main quantities of interest are then given by

$$\langle\eta_{ice}^2\rangle = m_0[\eta_{ice}], \quad \langle\varepsilon^2\rangle = m_0[\varepsilon], \quad T_W = 2\pi\sqrt{\frac{m_0[\eta_{ice}]}{m_2[\eta_{ice}]}}. \tag{9}$$

If $k_W = k_{ice}(2\pi/T_W)$ is the real part of the wavenumber κ when the period is T_W, the dominant wavelength referred to earlier is given by $\lambda_W = 2\pi/k_W$. The probability of the strain amplitude exceeding the breaking strain ϵ_c is

$$\mathbb{P}_\varepsilon \equiv \mathbb{P}(E_W > \varepsilon_c) = \exp\left(\frac{-\varepsilon_c}{2\langle\varepsilon^2\rangle}\right). \tag{10}$$

3.2. Breaking criterion

To determine whether the ice will be broken by waves, we define a critical probability threshold $\mathbb{P}_c$ such that if $\mathbb{P}_\varepsilon > \mathbb{P}_c$ the ice will break. If it breaks, the maximum floe size is set to $D_{max} = \max(\lambda_W/2, D_{min})$ where D_{min} is the size below which waves are not significantly attenuated and is set to 20 m (Kohout and Meylan, 2008). These two quantities, D_{min} and D_{max}, determine the FSD (see Section 4.1 of Part 1).

From (10), the criterion $\mathbb{P}_\varepsilon > \mathbb{P}_c$ can be written in terms of E_s, ε_c and $\mathbb{P}_c$ as

$$E_s > E_c = \varepsilon_c\sqrt{-2/\log(\mathbb{P}_c)}. \tag{11}$$

Thus the single parameter E_c combines the effects of both ε_c and $\mathbb{P}_c$. Consequently, testing the sensitivity of the WIM to E_c allows for the combined effects of our choice of $\mathbb{P}_c$ and also of uncertainties in the breaking strain ε_c, which are considerable. Note that if $\mathbb{P}_c = e^{-1} \approx 0.37$, the breaking criterion becomes $E_s > \varepsilon_c\sqrt{2}$, which is the same as for a monochromatic wave.

3.3. Floe size distribution

Following DKB and Toyota et al., 2011, we use a fractal breaking model that predicts the FSD from D_{max} and D_{min}. We assume floes that break produce ξ^2 pieces, and that the fragility of the floes (the probability that a floe will break) is fixed at Π. We use $\xi = 2$ and $\Pi = 0.9$.

We determine the mean floe size from the formula of DKB:

$$\langle D\rangle = \frac{\sum_{m=1}^M (\xi\Pi)^m}{\sum_{m=1}^M (\xi^2\Pi)^m}, \quad M = \lfloor\log_\xi(D_{max}/D_{min})\rfloor, \tag{12}$$

where $\lfloor\cdot\rfloor$ denotes rounding down to the nearest integer. The FSD is discussed in more detail in Section 4.1 of Part 1.

4. Wave energy transport in the MIZ

4.1. Continuous equations

The energy balance equation for waves in the ice-covered ocean is

$$\frac{1}{c_g}D_t S(\omega; x, t) = R_{in} - R_{ice} - R_{other} - R_{nl}, \tag{13}$$

(Masson and LeBlond, 1989; Meylan and Masson, 2006; Ardhuin et al., 2010), where c_g is the group velocity and $D_t \equiv (\partial_t + c_g\partial_x)$. The source terms R_{in}, R_{ice} and R_{other} represent, respectively, the wind energy input, rates of energy loss to (or due to) the sea ice and the total of all other dissipation sources (e.g., friction at the bottom of the sea, losses from wave breaking or white-capping, Ardhuin et al., 2010). These are all quasi-linear in S. The R_{nl} term incorporates fully non-linear energy exchanges between frequencies (Hasselmann, 1962; Hasselmann, 1963).

In the present study we consider only wave attenuation caused by the presence of ice cover. Our simplified equation is therefore

$$\frac{1}{c_g}D_t S(\omega; x, t) = -R_{ice} \approx -\hat{\alpha}(\omega, x, t)S(\omega; x, t), \tag{14}$$

where $\hat{\alpha}$ is the dimensional attenuation coefficient, i.e., the rate of exponential attenuation per meter. We model the wave attenuation as being the sum of linear wave scattering at floe edges and a viscosity term; this is discussed in detail in Section 4.2 of Part 1. The attenuation coefficient is not explicitly dependent on S, but changes suddenly when the wave energy (or more specifically the significant strain E_s) becomes large enough to cause ice breakage. This added subtlety is unique to our model and its predecessor DKB.

As discussed in Section 3.1 of Part 1, Eq. (14) represents advection of S at the group velocity c_g followed by its attenuation using $\hat{\alpha}$. This can be seen by considering the above problem, between breaking events, in the Lagrangian frame. The resulting expressions are

$$\frac{dx}{dt} = c_g(\omega, x, t_*) \quad \text{and} \tag{15a}$$

$$\frac{d}{dx}S(\omega; x, t) = -\hat{\alpha}(\omega; x, t_*, S_*)S(\omega; x, t), \tag{15b}$$

where t_* is the last time breaking occurred at x, and $S_*(\omega; x) = S(\omega; x, t_*)$. Thus, we have separated the problem into an

advection problem (in which we solve $D_tS = 0$) and an attenuation one. In our numerical scheme presented in the next section, we solve (14) by alternately advecting and attenuating.

4.2. Full numerical implementation

Let us discretize our space, time and frequency variables using

$$\text{Space}: \quad x_j = j\Delta x \quad (j = 0, 1, \ldots, N_x),$$
$$\text{Time}: \quad t_n = n\Delta t \quad (n = 0, 1, \ldots, N_t),$$
$$\text{Frequency}: \quad \omega_r = \omega_0 + r\Delta\omega \quad (r = 0, 1, \ldots, N_\omega).$$

We choose ω_0 and $\Delta\omega$ so that 31 periods between 2.5 s and 25 s are included. For all temporal indices n, spatial indices j and frequency indices r, we use the shorthand notations

$$c_j = c(x_j), \qquad\qquad h_j = h(x_j),$$
$$c_{\mathrm{g},r} = c_\mathrm{g}(\omega_r), \qquad\qquad S_{j,r}^n = S(\omega_r, x_j, t_n),$$
$$D_j^n = D_{\max}(x_j, t_n), \quad \langle D_j^n \rangle = \langle D \rangle(x_j, t_n).$$

The Courant number is $(\mathcal{C})_r \equiv c_{\mathrm{g},r}\Delta t/\Delta x \in (0, 1]$ (for $r = 0, 1, \ldots, N_\omega$). It represents the proportion of one grid cell a wave of a given frequency travels in one time step.

For $j = 1, \ldots, N_x$, we also let

$$W_{j,r} = W(\omega_r), \quad E_{j,r} = E(\omega_r), \tag{16}$$

observing that we will need these to approximate the integrals (8). Note that W and E have an implicit dependence on the ice properties, which is why $W_{j,r}$ and $E_{j,r}$ depend on the index of the grid cell as well as the frequency index.

Following DKB, our numerical implementation (which we call N1) proceeds as follows.

1. *Initialization.* For $r = 0, 1, \ldots, N_\omega$:
   We initialise the problem by setting the incident wave spectrum and initial FSD to:

$$S_{j,r}^0 = \begin{cases} S_B(\omega_r; T_\mathrm{p}, H_\mathrm{s}) & \text{for } j = 0, 1, 2, \\ 0 & \text{for } j = 3, 4, \ldots, N_x, \end{cases} \tag{17a}$$

$$\text{and} \quad D_j^0 = \langle D_j^0 \rangle = \begin{cases} D_\mathrm{init} & \text{if } c_j > 0, \\ 0 & \text{if } c_j = 0. \end{cases} \tag{17b}$$

Here D_init is an arbitrarily chosen (relatively large) value. By invoking (17b) at $j = 0, 1, 2$, we can apply (2) via the Neumann condition $\partial_x S(\omega, 0, t) = 0$ during the advection step. Note that this implies $\partial_t S(\omega, 0, t) = 0$, since the advection equation is $D_t S = 0$. We need three points initially constant, as we advect S using a second order method.

2. *Time integration.* For $n = 1, 2, \ldots, N_t$:
   For $r = 0, 1, \ldots, N_\omega$:
   (i) *Advection.* In our integration we alternate between advection and attenuation. The advection is done by solving the equation $D_t S = 0$ using the Lax-Wendroff scheme (a second order direct space–time method) with Superbee flux limiting (Roe, 1986) and a Neumann boundary condition, as mentioned above. The scheme is stable for Courant number $\mathcal{C}_r \in (0, 1]$ and has very little numerical diffusion for $0.1 \lesssim \mathcal{C}_r < 1$. We perform the advection over the whole domain in one step, mapping $S_{j,r}^{n-1}$ onto an unattenuated intermediate spectrum $\hat{S}_{j,r}^n$ ($\forall j = 1, 2, \ldots, N_x$).
   For $j = 1, 2, \ldots, N_x$:
   We now apply attenuation and the subsequent integration over frequency locally, i.e., we consider each cell separately. We reset $m_0[\eta_\mathrm{ice}] = m_2[\eta_\mathrm{ice}] = m_0[\varepsilon] = 0$, and these integrals are calculated cumulatively as we loop through the frequencies. For $r = 0, 1, \ldots, N_\omega$:
   (ii) *Attenuation.* We calculate the attenuation coefficient and the attenuated wave spectrum to be

$$\hat{\alpha}_{j,r}^n = \frac{\alpha_{j,r}c_j}{\langle D_j^{n-1} \rangle} \quad \text{and} \tag{18a}$$

$$S_{j,r}^n = \hat{S}_{j,r}^n \exp\left(-\hat{\alpha}_{j,r}^n c_{\mathrm{g},r}\Delta t\right), \tag{18b}$$

where $\alpha_{j,r} = \alpha(x_j, \omega_r)$ is the non-dimensional attenuation coefficient (cf. Section 3.1 of Part 1).
(iii) *Integration over frequency.* The integrals over frequency are approximated using Simpson's rule, i.e.,

$$\int_0^\infty f(\omega)\mathrm{d}\omega \approx \int_{\omega_0}^{\omega_{N_\omega}} f(\omega)\mathrm{d}\omega \approx \sum_{r=0}^{N_\omega} w_r f(\omega_r). \tag{19}$$

Thus we can update the integrals we need as the r loop proceeds:

$$m_0[\eta_\mathrm{ice}] = m_0[\eta_\mathrm{ice}] + w_r S_{j,r}^n W_{j,r}^2; \tag{20a}$$

$$m_2[\eta_\mathrm{ice}] = m_2[\eta_\mathrm{ice}] + w_r \omega_r^2 S_{j,r}^n W_{j,r}^2; \tag{20b}$$

$$\text{and} \;\; m_0[\varepsilon] = m_0[\varepsilon] + w_r S_{j,r}^n E_{j,r}^2. \tag{20c}$$

(iv) *Floe breaking.* Having completed the frequency integration, the significant strain, E_s and the dominant period T_W is obtained from (4) and (9) following Section 3.2 of Part 1. If $E_\mathrm{s} > E_\mathrm{c} = \sqrt{2}\varepsilon_\mathrm{c}$, the ice breaks, and we reduce the maximum floe size to $D_j^n = \max\{D_\mathrm{min}, \min\{\lambda_\mathrm{W}/2, D_j^{n-1}\}\}$, where $\lambda_\mathrm{W} = 2\pi/k_\mathrm{ice}(2\pi/T_\mathrm{W})$ is the wavelength corresponding to T_W and the ice properties in the cell. We then calculate the new average floe size $\langle D_j^n \rangle$ from (12).

3. *Define the MIZ.* At the end of the integration, the point x_j is defined to be inside the MIZ if the corresponding cell contains ice and if ice breakage has occurred in that cell, i.e., if $0 < D_j^{N_t} < D_\mathrm{init}$ ($j = 0, 1, \ldots, N_x$). The MIZ width, L_MIZ, is then the distance from the ice edge to the last point in the MIZ, which includes any internal polynyas. We also define D_MIZ as the maximum floe size in this region.

If $\mathcal{C}_r = 1$ the waves travel one grid cell every time step and hence do not experience any attenuation from any ice they break, as the broken ice is always behind them. However, if $\mathcal{C}_r < 1$, waves travel less than a grid cell per time step and must therefore pass through a proportion of this broken ice before escaping the cell. This is because we use a *well-mixed* grid cell, as opposed to a partial grid cell. The proportion of broken ice the wave must pass through in a grid cell is $1 - \mathcal{C}_r$, i.e., it increases as the Courant number $\mathcal{C}_r$ decreases. In our numerical results we will show that the FSD is insensitive to the exact amount of broken ice the waves travel through if the maximum Courant number $\mathcal{C} = \max\{\mathcal{C}_r | r = 0, 1, \ldots, N_\omega\}$ is less than approximately $\mathcal{C} \lesssim 0.7$. This represents an equilibrium between the wave field and the FSD, which will be discussed in Section 4.3. In addition, while the scheme depends on the initial floe size D_init for $\mathcal{C} \approx 1$, it does not in the limit $\mathcal{C} \to 0$, and therefore for $\mathcal{C} \lesssim 0.7$.

4.3. Semi-analytical schemes

The N1 scheme described in the previous section is a general numerical implementation of the WIM that is applicable to any ice and wave conditions. In particular, it can deal with wave dispersion (wave speed dependent on frequency), and it is generalizable to two horizontal dimensions. However, if we neglect dispersion we can derive semi-analytic methods for the $\mathcal{C} \to 1$ and the $\mathcal{C} \to 0$ limits. The purpose of doing this is twofold: (i) to check our numerical method; and (ii) to produce a much faster algorithm to determine MIZ width, as the frequency loop is only inside a single spatial loop instead of being within both spatial and temporal loops (as in the N1 algorithm). Of course, if we wish to know the wave spectrum at a particular time in the ice—for

example, if we wish to know when a group of large waves will reach a certain point, dispersive effects must be considered. Notwithstanding, it will be shown in Section 5.1 that the predicted FSD is insensitive to the effects of wave dispersion. Finally, we note that generalizing semi-analytical methods to the two-dimensional situation is challenging and that the numerical model is necessary to overcome the added complexity of the extra dimension. When we set $\mathcal{C}_r = 1$ for all r in the N1 scheme, all of the ice breakage is caused by the lead waves as they always travel through unbroken ice. The waves do not suffer additional attenuation due to floes that have been freshly broken. Accordingly, in this situation it is possible to calculate the breaking penetration, and hence the width of the MIZ, just by considering the attenuation of the lead waves (referred to hereinafter using the superscript 'lw'). We denote the semi-analytic method that reproduces the $\mathcal{C}_r \to 1$ $(r = 0, 1, \ldots, N_\omega)$ limiting case by A1. This method is essentially the same as that of Vaughan and Squire, 2011. The wave spectrum when the lead wave is at a given position x is given explicitly by

$$S^{lw}(\omega, x) = S(\omega, 0, 0) \exp\left(-\int_0^x \hat{\alpha}(\omega, x', 0) dx'\right). \tag{21}$$

We can also calculate the moments for the lead wave

$$m_\varepsilon^{lw}(x) = \int_0^\infty S^{lw}(\omega, x) E^2(\omega) d\omega \quad \text{and} \tag{22a}$$

$$m_n^{lw}(x) = \int_0^\infty \omega^n S^{lw}(\omega, x) W^2(\omega) d\omega, \tag{22b}$$

which give us the significant strain and the dominant wave period:

$$E_s^{lw}(x) = 2\sqrt{m_\varepsilon^{lw}(x)}, \quad \text{and} \quad T_W^{lw}(x) = 2\pi\sqrt{\frac{m_0^{lw}(x)}{m_2^{lw}(x)}}.$$

We can then find the width of the MIZ, i.e., the distance over which the ice cover is broken, L_{MIZ}, by solving $E_s^{lw}(L_{MIZ}) = E_c$. In practice, we still discretize the problem as before to calculate the integral (21) in which $\hat{\alpha}$ varies spatially, but we no longer have to consider the time dimension. The FSD is calculated as a function of x from the wavelength corresponding to $T_W^{lw}(x)$.

The precise A1 algorithm proceeds as follows.

1. *Initialization.* For $r = 0, 1, \ldots, N_\omega$, $j = 0, 1, \ldots, N_x$:
   We set the incident wave spectrum and initial FSD to be

$$S_{0,r}^{lw} = S_B(\omega_r; T_p, H_s), \tag{23a}$$

$$\text{and} \quad D_j^0 = \left\langle D_j^0 \right\rangle = \begin{cases} D_{init} & \text{if } c_j > 0, \\ 0 & \text{if } c_j = 0. \end{cases} \tag{23b}$$

2. *Propagation of the lead waves.* For $j = 1, 2, \ldots, N_x$: Reset the following integrals to zero: $m_0^{lw}[\eta_{ice}] = m_2^{lw}[\eta_{ice}] = m_0^{lw}[\varepsilon] = 0$.
   For $r = 0, 1, \ldots, N_\omega$:
   (i) *Advection.* The waves move from one grid cell to the next without the effects of time-stepping and the Courant number $\mathcal{C}$:

$$\hat{S}_{j,r}^{lw} = S_{j-1,r}^{lw}. \tag{24}$$

   (ii) *Attenuation.* We calculate the dimensional attenuation coefficient from the initial FSD, so breaking effects do not influence the transmission of the waves. The energy S is also reduced accordingly at this point.

$$\hat{\alpha}_{j,r} = \frac{\alpha_{j,r} c_j}{\left\langle D_j^0 \right\rangle}, \quad \text{and} \tag{25a}$$

$$S_{j,r}^{lw} = \hat{S}_{j,r}^{lw} \exp\left(-\hat{\alpha}_{j,r} \Delta x\right). \tag{25b}$$

   (iii) *Integration over frequency.* We update the integrals that we need

$$m_0^{lw}[\eta_{ice}] = m_0^{lw}[\eta_{ice}] + w_r S_{j,r}^{lw} W_{j,r}^2, \tag{26a}$$

$$m_2^{lw}[\eta_{ice}] = m_2^{lw}[\eta_{ice}] + w_r \omega_r^2 S_{j,r}^{lw} W_{j,r}^2, \tag{26b}$$

$$\text{and} \quad m_0^{lw}[\varepsilon] = m_0^{lw}[\varepsilon] + w_r S_{j,r}^{lw} E_{j,r}^2. \tag{26c}$$

   (iv) *Floe breaking.* Having finished the frequency (r) loop, we can calculate E_s^{lw} and T_W^{lw} from (26c). If $E_s^{lw} > E_c$ then the ice breaks, giving a maximum floe size $D_j^{lw} = \max\{D_{min}, \min\{\lambda_W^{lw}/2, D_j^0\}\}$, where λ_W^{lw} is the wavelength corresponding to T_W^{lw} and the thickness h_j. Calculate the new average floe size $\langle D_j^{lw} \rangle$.

3. *Define the MIZ.* When the lead waves have left the domain, i.e., after the j loop has been completed, we can define the MIZ as in the N1 scheme.

We denote the scheme that approximates the FSD in the $\mathcal{C} \to 0$ limit by A0. It is produced by reversing the order in which we apply breaking and attenuation in the A1 scheme. More precisely, we move the attenuation loop over r (A1 algorithm, step 2.ii) to after the breaking step (A1 algorithm, step 2.iv) and replace (25a) with

$$\hat{\alpha}_{j,r} = \frac{\alpha_{j,r} c_j}{\langle D_j^{lw} \rangle}. \tag{27}$$

Under the A1 scheme, the lead waves travel through the ice relatively unhindered, leaving broken ice in their path. The energy they lose is due to viscous damping and scattering at the relatively few floe edges they meet on their way, which is inversely proportional to the initial floe size D_{init}. Under the A0 scheme, the waves at a certain point have the same energy as if they had to travel through all the broken ice they produce. Therefore, the wave spectrum inside the broken ice is the result of an equilibrium between attenuation and breaking and is more stable.

An issue that is related to the two limiting cases is the amount of energy lost due to ice breakage. The A1 FSD is one extreme in which no energy is lost during this process. The A0 FSD is another critical point where the result of the amount of energy being lost is the same as the attenuation loss due to propagating through any broken floes that the waves themselves produce. Note that, if even more wave energy than this is lost, the MIZ due to the lead waves will initially be much narrower than the A0 MIZ, but following waves will gradually extend it towards the A0 limit. If less than this amount is lost during ice breakage, then we will be able to tell how sensitive the FSD is to the exact amount by testing the sensitivity of the N1 results to the $\mathcal{C}$ parameter, which moves the N1 FSD between the A1 and A0 limits.

5. Results

Table 1 lists the default model parameter values used in all simulations, unless otherwise specified. Attenuation model B from (Bennetts and Squire, 2012) is used with the default value of the viscous damping parameter, $\Gamma = 13$ Pa s m^{-1}. In the idealized simulations of Sections 5.1 and 5.2 we use the thickness and concentration profiles of (1) (also see Fig. 1).

5.1. Sensitivity to the Courant number, dispersion and horizontal resolution

Fig. 2 presents the model sensitivity of the different numerical schemes to the Courant number in the case where dispersion is neglected, i.e., $\mathcal{C}_r = \mathcal{C} \, \forall r = 0, 1, \ldots, N_\omega$. Fig. 2(a) shows values of D_{max} along a transect. Results are produced by the numerical scheme N1, in which the waves travel through proportions 0, 0.01, 0.05, 0.1 and 0.3 of the ice they break (i.e., with Courant numbers $\mathcal{C} = 1, 0.99, 0.95, 0.9$ and 0.7). Results are compared to those obtained by the two semi-analytical schemes A1 and A0. N1 and A1 agree exactly when $\mathcal{C} = 1$ while N1 and A0 agree as $\mathcal{C}$ decreases.
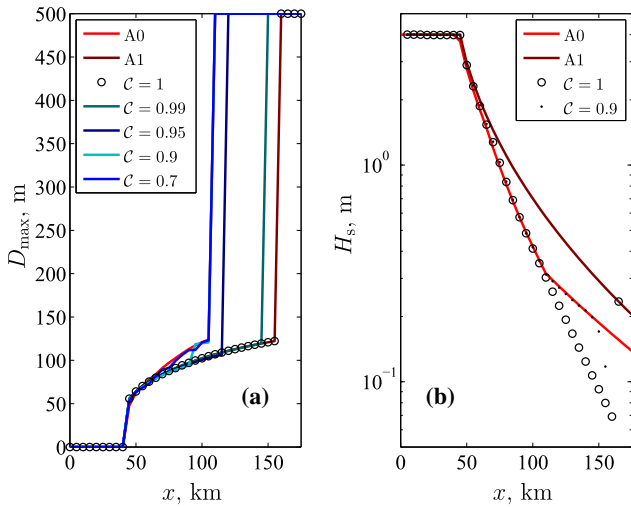
Fig. 2. General properties of the WIMs. Dispersion is neglected, the incident wave spectrum has $T_p = 9.5$ s, and the ice thickness used in (1a) is $h_\infty = 4$ m. (a) Values of D_{max} after using the A0 and A1 semi-analytic schemes, or the N1 scheme with the indicated values of $\mathcal{C}$. (b) Significant wave height at time $t = 2.02$ h.

Fig. 3. Behaviour of numerical scheme N1 with maximum CFL number, $\mathcal{C}$, and comparision with the A0 and A1 semi-analytic schemes. (a, b) Dispersion is neglected. The ice thickness used comes from equation (1a) with $h_\infty = 4$ m. (c, d) Dispersion is included. The ice thickness used is $h_\infty = 2$ m.

Fig. 2(b) shows a snapshot in time of the significant wave height as the waves travel further into the ice. We only show results for N1 with $\mathcal{C} = 1$ and 0.9, and the semi-analytical schemes A1 and A0 in this case. We see that H_s under the A1 scheme decreases slowly and smoothly as the lead waves travel into the ice, only being attenuated by unbroken ice. In contrast, under the A0 scheme, when the lead waves must travel through all the ice that they break, the significant wave height decreases rapidly due to the broken ice, until about $x = 110$ km. This represents the end of the A0 MIZ, where the waves reach unbroken ice and H_s drops less rapidly.

Under the N1 scheme with $\mathcal{C} = 1$, we can see that, as expected, the lead wave (the right-most circle) tracks the A1 curve exactly. However, the following waves have heights that are several orders of magnitude smaller. Inside the A0 MIZ, H_s for these waves tracks the A0 curve, but drops below it outside this region. This is because the lead wave with this Courant number is still able to break ice outside the A0 MIZ, so the following waves are still traveling through broken ice.

When $\mathcal{C}$ drops to 0.9, the wave heights under the N1 scheme follow the A0 ones almost exactly. Only the two right-most points (black dots) drop below the A0 curve as numerical error from the advection algorithm begins to take effect. The A0 wave heights thus represent a kind of steady-state or equilibrium solution.

In addition to the above, the following conclusions can be inferred from the results. First, the significant wave heights predicted by the N1 scheme for all Courant numbers agree for the interval in which they share broken ice, i.e., before the edge of the MIZ under the A0 scheme. Second, D_{MIZ} is not sensitive to the Courant number for the N1 scheme, but L_{MIZ} in the A1 and A0 limits consistently differs by a factor of about 1.6. However, the MIZ width rapidly drops to the A0 value even for N1 with $\mathcal{C} = 0.9$. That is, below a certain value, L_{MIZ} is insensitive to $\mathcal{C}$. As we expect that a significant amount of wave energy will be lost during the breaking process, this indicates little sensitivity to the precise quantity lost, explored here by varying the Courant number.

In Fig. 3(a) and (b) we further investigate the sensitivity of N1 to the Courant number as a proxy for energy loss. Results are shown for both the maximum floe size, D_{MIZ}, and the width of the MIZ L_{MIZ} as functions of the peak period, for a maximum ice thickness of $h_\infty = 4$ m. It is again evident that the results of N1 converge rapidly to those of A0, as the Courant number decreases.
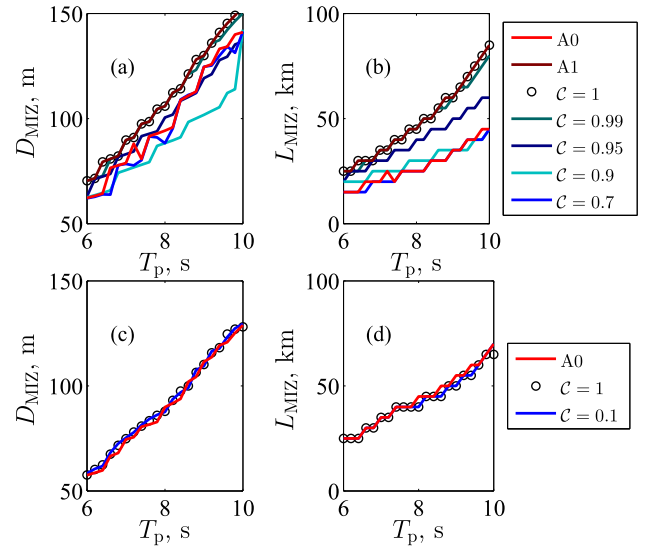
In Fig. 3(c) and (d) we test the effect of allowing dispersion. Results are presented for maximum Courant numbers $\mathcal{C} = 1$ and 0.1. The semi-analytical A0 scheme is also shown, and both N1 curves lie almost exactly upon it. Thus D_{MIZ} and L_{MIZ} display very little sensitivity to dispersion and when it is included the results are essentially independent of $\mathcal{C}$. As noted in Section 4.3, this is an extremely useful result for computational efficiency in the later results of this paper.

Two key conclusions can be drawn from Figs. 2 and 3. First, the numerical scheme is not very sensitive to the energy lost during ice breakage (parameterized by the Courant number) with the current floe breaking parameterization. Second, dispersion is not necessary to calculate the FSD. Consequently, it is valid to use the numerically efficient A0 scheme to test the sensitivity of the model to the ice properties (Section 5.2) and for the realistic simulations presented in Section 5.3.
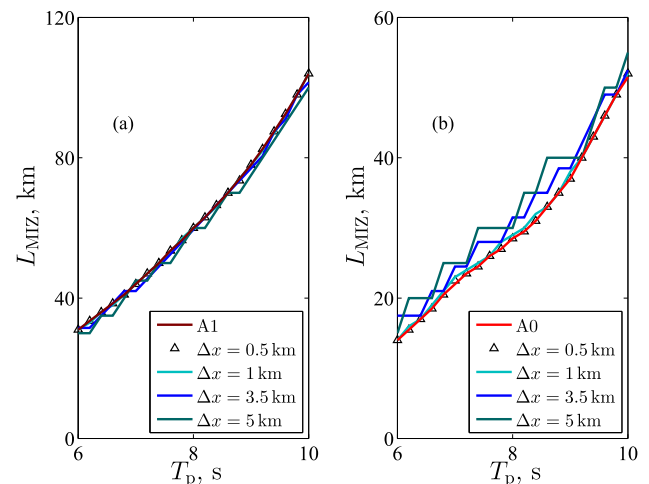

Fig. 4. Behaviour of numerical schemes with grid size, Δx. (a) Value of L_{MIZ} after using scheme A1 ($\Delta x = 0.5$ km), or N1 with $\mathcal{C} = 1$ and the indicated values of Δx; (b) Same as (a), but with scheme A0 instead of A1, and N1 used with $\mathcal{C} = 0.7$ instead of 1. The ice thickness used in (1a) is $h_\infty = 3$ m.

The final numerical issue that we investigate is the spatial resolution. Fig. 4 shows the convergence of the two numerical schemes as the default grid size $\Delta x = 5$ km is reduced ten-fold. The MIZ width L_{MIZ} converges a lot faster with $\mathcal{C} = 1$ than with $\mathcal{C} = 0.7$. However, the latter only overestimates L_{MIZ} by about one or two grid cells, so using $\Delta x = 5$ km will not produce significant inaccuracies. High resolution ice-ocean models generally have grid sizes of about 2–4 km, while coarser models use approximately 10–20 km. In both cases the errors should be well below the noise level as the ice edge can be incorrectly located by as much as 40 km in contemporary models.

5.2. Sensitivity to wave attenuation and ice properties

We first revisit Figs. 3 and 4 to investigate the sensitivity of MIZ width to the ice thickness. Comparing the red A0 curves in Figs. 3(d) and 4(b), we see that L_{MIZ} for $h_\infty = 2$, 3 and 4 m is respectively about 15, 17 and 25 km when $T_p = 6$ s, and about 48, 55 and 75 km when $T_p = 10$ s. Thus doubling the thickness increases the MIZ width by a factor of approximately 1.6. Thickness observations are much more difficult to obtain than measurements of properties such as concentration, so ice models rarely assimilate thickness. As a result model predictions for thickness can be quite inaccurate. Accordingly, the high sensitivity of our results to thickness is of potential concern. Notwithstanding, the realistic simulations presented in the following section do not show such high variability with changes to thickness.

Figs. 5(a) and (b) show the effect of varying the damping parameter Γ in attenuation model B on the width of the MIZ predicted by our WIM. As expected, without the extra damping, i.e., when $\Gamma = 0$, waves can penetrate further into the ice-covered ocean and cause more ice breakage. The change is most pronounced for large values of the incident peak period. This is because scattering dominates the attenuation rate for small to medium values of wave period. The largest sensitivity of the width of the MIZ to Γ is for the simulation with thinner ice, shown in panel (a). This is because the flexural rigidity F in (6) is proportional to h^3, so it quickly begins to dominate Γ at larger thicknesses, reducing the damping effect (also see the discussion in Appendix A of Part 1).

We further note that the prediction of L_{MIZ} for larger values of Γ is less sensitive to changes in thickness. In these results doubling the thickness roughly halves the MIZ width when $\Gamma = 0$, but only reduces it by a factor of approximately 1.6 when $\Gamma = 13$ Pa s m^{-1}.

Fig. 5(c) shows the effect of changing the ice concentration on the width of the MIZ. Doubling the concentration, for example, doubles the number of floe edges and thus doubles the attenuation coefficient. We may, therefore, expect this to cause L_{MIZ} to change by a factor of a half. However, the drop in L_{MIZ} in going from $c_\infty = 0.25$ to $c_\infty = 0.5$ is approximately 25% rather than 50%, and in going from $c_\infty = 0.25$ to $c_\infty = 0.75$ is approximately 50%, rather than 66%. The results therefore do not behave as simply as one can anticipate for a single monochromatic wave. In reality it represents the combined action of non-linear effects arising by considering a wave spectrum and feedback between attenuation and ice breakage.

In Fig. 5(d), we test the sensitivity to the breaking strain parameter E_c. This parameter incorporates the effect of the absolute breaking strain ε_c, the probability threshold $\mathbb{P}_c$ directly, and implicitly the incident significant wave height H_s. Since the Bretschneider spectrum is proportional to H_s^2, the significant strain will be approximately proportional to H_s. Thus doubling H_s will have about the same effect as halving the breaking strain E_c.

Choosing $\mathbb{P}_c = 0.01$, $e^{-2} \approx 0.1$, $e^{-1} \approx 0.37$, or $e^{-2/9} \approx 0.8$ (respectively) makes $\beta_\varepsilon = E_c/E_c^{(0)} = 0.47$, 0.7, 1, or 2.1, where $E_c^{(0)} = \varepsilon_c\sqrt{2} \approx 7.05 \times 10^{-5}$ is our default value, which is consistent with the limit for monochromatic waves (see Section 3.2.2 of Part 1). Testing values of β_ε between 1/3 and 3 should cover most reasonable variations in $\mathbb{P}_c$, and also our uncertainties in the values of ε_c and H_s. This range gives variations of about 50%. Again though, when we move to more realistic tests where the different variables interact in more complicated ways, there is generally a lot less variation with β_ε than is observed here.

5.3. Realistic experiments in the Fram Strait

Here we repeat some of the sensitivity studies in simulations using the A0 scheme with realistic wave forcings, ice concentrations and ice thicknesses along a transect of the Fram Strait during 2007. Fig. 6 shows a map of the area and the location of the transect. It also shows the location of the grid cell where wave forcing data was extracted from the WAM ERA-Interim reanalysis. Fig. 7(a) shows a time series of this wave forcing, while Figs. 7(b) and (c)
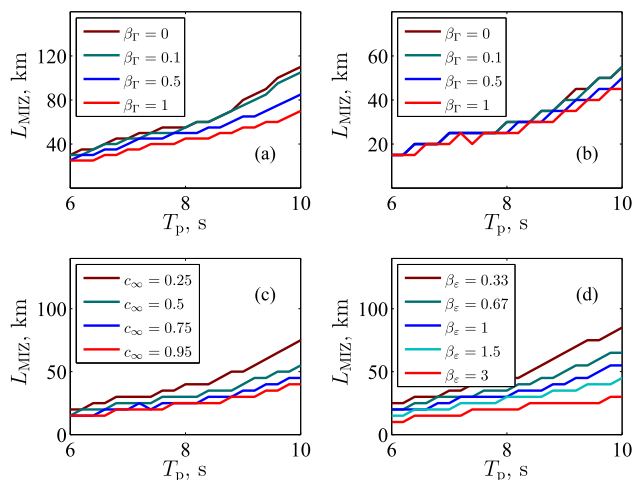

Fig. 5. The effect of the attenuation model and ice concentration. (a, b) Values of L_{MIZ} after using the semi-analytic scheme A0 and attenuation model B with $\Gamma = \beta_\Gamma \times 13$ Pa s m^{-1} and the indicated value of β_Γ. The ice thicknesses used in (1a) are $h_\infty = 2$ m (a) and $h_\infty = 4$ m (b). (c) Values of L_{MIZ} after using the A0 scheme with the indicated values of c_∞ used in (1b), and with $h_\infty = 2$ m in (1a). (d) The effect of the parameter E_c. Values of L_{MIZ} after using WIMA0 with $E_c = \beta_\varepsilon\sqrt{2}\varepsilon_c$, where $\varepsilon_c \approx 4.99 \times 10^{-5}$ and β_ε is indicated. The ice thickness used is $h_\infty = 3$ m.
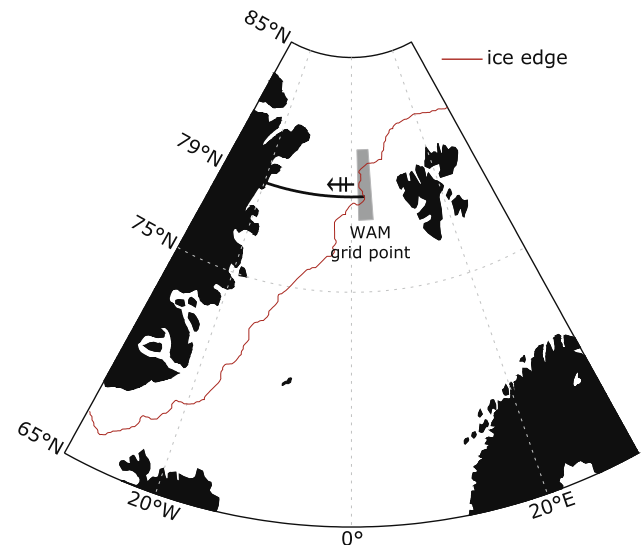

Fig. 6. Map of the Fram Strait area showing the observed ice edge on 7 November 2007. The thick black line along 79N shows the location where the ice parameters were extracted for the simulations; this is where the WIM is tested. The gray box shows the grid cell from which ocean wavefields were extracted from the WAM ERA-Interim reanalysis.

show, respectively, ice concentrations and thicknesses obtained from a TOPAZ reanalysis (Sakov et al., 2012) in which concentration data derived from the Ocean and Sea Ice Satellite Application Facility (OSI SAF, met.no) have been assimilated. On average, the modeled ice edge is 45 km west of the ice edge observed by AMSR-E (University of Bremen) and determined from the analysis of Kloster and Sandven (2011), which is plotted as a solid line in Fig. 7(b). This discrepancy is well within the uncertainties and resolution of the model (TOPAZ has a resolution of about 13 km) and the resolution of the AMSR-E analysis. (Kloster and Sandven, 2011, divided the transect from 15°W to 5°E into bins with widths of about 21.2 km, i.e. 1 degree in longitude, and analyzed them for ice concentration.) The internal concentrations from the model and the data also compare well.

Also plotted (dashed line) in Fig. 7(b) is an estimate for the inner edge of the MIZ, determined from the same AMSR-E concentrations using the criterion that $c < 0.9$ corresponds to the MIZ. While this is a different criterion from the floe size criterion, where we define the MIZ by whether the ice is broken or not—see step 3 of the N1 algorithm in Section 4.2 we use in this paper—it provides a rough estimate of the accuracy of the predictions obtained from our WIM (Strong, 2012).

The mean ice thickness is roughly 0.8 m, creeping up towards 2 m in the summer, which is thicker due to greater movement south of multi-year ice from the Arctic Ocean at that time. According to Widell et al., 2003, these ice thicknesses are probably too low, so we have also run simulations in which the ice thicknesses are multiplied by a factor $\beta_h = 1.75$ or 2.5 in order to get closer to observations. We observe that the Fram Strait is a particularly challenging MIZ to model, as it is made up of sea ice that is continuously being channeled out of the Arctic Basin, locally-growing sea ice in winter, and liberated land fast ice that can include sikussak. It is also baroclinically unstable so its edge is often characterized by the presence of many eddies and meanders.

Fig. 8 shows the results of numerical experiments using the model outlined in this work. Results for the expected ice breakage are calculated daily using either the TOPAZ thicknesses or the increased thicknesses, the TOPAZ concentrations and the ERA-Interim waves. Floe sizes are re-initialized for each model pass to be uniformly $D_{init} = 500$ m long. An extension to include a memory in each cell of D_{max} and a gradual refreezing was rejected on the basis that we are unable to embed the more important effects of ice movement due to winds and current into this one-dimensional experiment.

Figs. 8(a) and (c) show the results when attenuation model B is used with $\Gamma = 13$ Pa s m^{-1}. The variations are systematic in that increasing the thickness or breaking strain makes the MIZ narrower. For the winter months, MIZ widths estimated from our ice breakage model are about half the widths determined from the AMSR-E-measured concentrations. In the summer, when the wave heights are much lower and the ice is thicker, there is a lot less ice breakage, whereas the concentration criterion defines the MIZ as being much larger than the winter. This could be due to the more dilute ice being able to spread out even further in response to stresses from off-ice winds and currents. The neglected effect of ice advection would thus become more important in this period as well.

Fig. 8(a) shows the variation of the MIZ width with thickness. There is more variation in the summer when the ice is already very thick. However, in the winter, the variations are much reduced, both in comparison with the summer variability and the idealized results of the previous section.

Fig. 8(c) shows that the MIZ width responds to variations in the breaking strain in a similar way that it did to thickness variations. Again, there is significantly more variation in the summer, but the winter results are much less sensitive than they would be expected to be from idealized experiments.

Fig. 8(b) shows that the biggest source of variability comes from the choice of viscosity parameter Γ. When $\Gamma = 0$, maxima in the winter MIZ widths (reflecting days with strong incident wave fields) often reach about 0.8–1.0 times the AMSR-E widths, but are generally about one half to one third of them. The noise in the curves reflects the day-to-day variations in the incident wave fields. In the summer, all three values of Γ predict very low widths due to the weak incident waves. With Γ increased to 6.5 Pa s m^{-1}, the values of L_{MIZ} drop and become much closer to the widths
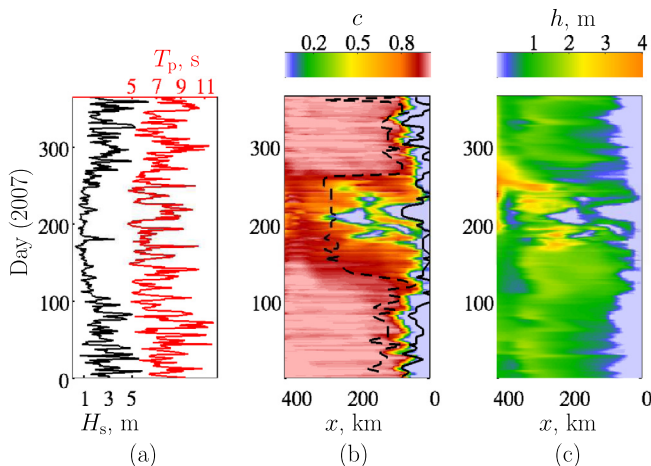

Fig. 7. Model data for our one-dimensional simulations in the Fram Strait in 2007, between the south-east coast of Norske Øer (latitude 79°N, longitude 17.7°W), which corresponds to $x = 438$ km on our one-dimensional grid, and latitude 79°N, longitude 3°E, which corresponds to $x = 0$. The wave field is specified at $x = 0$ and is obtained from the WAM ERA-Interim reanalysis. The significant wave heights and peak periods are plotted in (a). The waves are then advected west through ice with concentrations and thicknesses taken from a TOPAZ reanalysis. They are interpolated onto a regular grid with longitudinal resolution of 0.125° ($\Delta x = 2.65$ km), and are plotted in (b) and (c). For comparison, the ice edge and edge of the MIZ estimated from AMSR-E concentrations are also plotted in (b) as solid and dashed black lines, respectively.
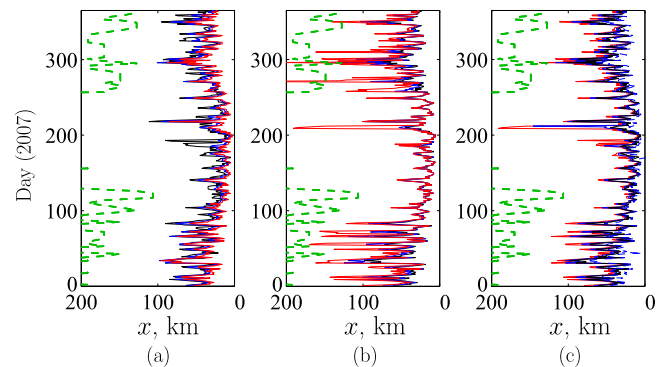

Fig. 8. Results of one-dimensional simulations in the Fram Strait in 2007. (a) L_{MIZ} determined by semi-analytical scheme A0 with $\beta_h = 1$ (–), $\beta_h = 1.75$ (–) and $\beta_h = 2.5$ (–), where β_h is a factor used to increase the ice thicknesses from Fig. 7(c), which are unrealistically low. The breaking strain ε_c is 4.99×10^{-5}, determined from Part 1 (Section 4.3), using $v_b = 0.1$. (b) L_{MIZ} determined by WIMA0 using attenuation model B with $\beta_h = 1.75$ and $\Gamma = \beta_\Gamma \times 13$ Pa s m^{-1}, where $\beta_\Gamma = 0$ (–), $\beta_\Gamma = 0.5$ (–) and $\beta_\Gamma = 1$ (–). (c) L_{MIZ} determined by WIMA0 using attenuation model B with $\Gamma = 10$ Pa s m^{-1}, $\beta_h = 1.75$, and $E_c = 7.05\beta_\varepsilon \times 10^{-5}$, where $\beta_\varepsilon = 0.5$ (–), $\beta_\varepsilon = 0.75$ (–), $\beta_\varepsilon = 1$ (--) and $\beta_\varepsilon = 2$ (--). The factor β_ε is included to test the sensitivity to the breaking strain and other parameters such as the probability threshhold $\mathbb{P}_c$ and H_s. For comparison, the MIZ width estimated from AMSR-E concentrations is plotted as a dashed green line in all plots. (This is the distance between the two black lines in Fig. 7(b).)

produced by using $\Gamma = 13$ Pa s m^{-1}. This behaviour was also observed in the previous section, where results were variable with Γ when low values were used, but were more stable for Γ in the range 6.5–13 Pa s m^{-1}. The default value of 13 Pa s m^{-1} was chosen to make the attenuation of long waves match the measurements of Squire and Moore, 1980, as they can not be fully explained by present scattering theory. While low frequency measurements can have more noise in them, and more experiments to confirm these attenuation results are necessary, the stability of our results over the correct order of magnitude is encouraging.

Our results do, however, suggest that a (modeled) floe size criterion and a concentration criterion for the MIZ may give different predictions for its boundary. It is likely that a combination of the two should be used to model the large scale deformations of the ice. This emphasizes the need for more measurements of floe sizes and large scale deformations in the MIZ to determine how the two criteria are related and how they should be used to precisely define the MIZ. It is also highly likely that floe size and concentration are interlinked variables that will need to be consistently related to one another, once incorporated in a sea ice model. The above results also highlight the importance of obtaining a better understanding of the attenuation process and, in particular the lower-than-observed attenuation of long waves than is predicted by scattering theory. It also shows the urgent need for more measurements of attenuation and of more reliable thickness data.

6. Incorporating the WIM into coupled ice-ocean models

The WIM presented in this two-part paper is designed to be integrated into an ice/ocean model (IOM), such as HYCOM. Specifically, by WIM we mean the numerical scheme N1, as this is more easily generalized to two horizontal dimensions. The A0 and A1 schemes were implemented to provide checks for the N1 scheme in different limiting cases and also to provide fast results in this one-dimensional setting. However, it is much more difficult to generalize the semi-analytical schemes to two dimensions.

We envisage the WIM to be a separate module that is called periodically to update the floe size distribution (FSD). The wave model component of the IOM, e.g., WAM or WAVEWATCH III®, will provide the wave forcing boundary condition required in the WIM. The sea ice model component of the IOM, e.g., CICE, will provide the ice conditions for the WIM. We note that the quantities provided by the wave and sea ice models to the WIM are likely to require interpolation onto the high resolution grid it uses. The FSD computed by the WIM will be an input parameter for a number of other parameterizations in the IOM. For example, it can be used to distinguish between the pack ice and the MIZ, and thus to decide which large-scale rheology should be used to determine the ice deformation. The thermodynamic model of Steele (1992), for example, could also be applied to the FSD to allow for lateral melting (or freezing). We also note that the sub-components of the WIM (cf. Section 4 of Part 1) are independent and so, once the skeleton of the WIM is implemented, they can be easily updated whenever new data are obtained or new theoretical progress is made. The implementation of the WIM inside the TOPAZ operational analysis and forecasting system, which is based on the Hybrid Coordinate Ocean Model (HYCOM) and the sea ice model of Drange and Simonsen (1996), is in progress and will be the focus of a future manuscript. The sea ice model of Drange and Simonsen (1996) is similar to CICE.

7. Summary and overall conclusions

In Part 2 of this two-part series, we have developed the theory of wave-ice interactions, presented in Part 1, into a numerical algorithm that predicts the FSD and wave spectrum in the MIZ, given an incident wave spectrum at the ice edge, and ice thickness and surface concentration profiles. Our investigation focused on the predictions of the FSD.

The numerical WIM was outlined for one-dimensional transects, as a step towards the full two-dimensional model. But the restriction was also imposed to facilitate a thorough sensitivity study, with respect to the key numerical and physical parameters in the WIM. This is especially important because of the high degree of uncertainty in many of these quantities. Sensitivity studies were conducted, in the first instance, using idealized ice thickness and concentration profiles. The most substantive observations follow.

1. Sufficient convergence of the FSD is given by a spatial resolution of approximately 5 km.
2. The waves can be forced to travel through an arbitrary proportion of the ice they break by adjusting the Courant number in the time stepping component of the numerical algorithm. This serves as a proxy for wave energy lost during ice breakage. When the waves only travel through a small proportion of broken ice, small changes in the exact proportion can lead to large changes in the width of the MIZ. But, this sensitivity quickly reduces, and the MIZ width is unaffected by the exact proportion when the waves travel through more than 30% of the broken ice.
3. Neglecting dispersion of the wave spectrum does not affect the FSD predicted by the WIM. Semi-analytical models, which do not incorporate dispersion, were therefore proposed for the two limiting cases of wave energy loss during ice breakage. The semi-analytical models are numerically efficient and helped to validate the full numerical model. However, it was noted that it will be difficult to generalize these models to two-dimensions.
4. The FSD is highly sensitive to the values of the damping parameter Γ, the ice thickness, and the breaking strain parameter. This emphasizes the need for more measurements of ice thickness, wave attenuation and breaking strains, as well as *in situ* observations of ice breaking.

The WIM was also tested using realistic input parameters that represented the Fram Strait in 2007. The sensitivity of the FSD predicted by the WIM to the ice thickness and breaking strain parameter was lower than in the idealized simulations. However, sensitivity to Γ remained high. It is therefore crucial to resolve the problem of how long waves are attenuated theoretically, and also to conduct more experiments to confirm the observations of Squire and Moore (1980) and to extend them to different ice types.

To conclude, the MIZ widths obtained from the realistic simulations, i.e., the distance of broken ice in the model, were compared to MIZ widths determined from contemporaneous AMSR-E (University of Bremen) concentration data. In winter months, when waves are at their strongest, the MIZ widths predicted by the WIM were roughly half those predicted by the concentration criterion. In the summer, the model results and the concentration results give quite different boundaries to the MIZ. Probably this is partly due to smaller waves and thicker ice in this time period, partly to neglected effects like ice advection and thermodynamic effects, and partly due to the two different definitions of the MIZ. This highlights the need for more measurements of the FSD, and also more research on how to define the MIZ (in our case, for the purpose of determining which large-scale ice rheology to use) more precisely. The model proposed in this two-part series has been motivated by the many observations that suggest a primary role for ocean waves in shaping the morphology of ice fields. Waves habitually limit the size of the constituent ice floes throughout the MIZ, by fracturing those floes that are too large to exist as the waves permeate further into the ice pack. Attenuation, arising

due to scattering and supplementary inelastic processes such as turbulence, bending hysteresis and interfloe collisions and rafting, also occurs causing a gradual reduction of the wave energy envelope with distance from the ice edge that, *cæteris paribus*, results in a gradual increase in floe size with penetration. The FSD is therefore continuously modified by pervasive incident ocean wave trains that, according to their period, may either travel long fetches from distant storms or else be more locally generated. They are then preferentially filtered by the sea ice in a manner that favors the survival of longer wavelengths.

Given these several influential factors relating to the composition of MIZs, it is perhaps surprising to the reader that wave–ice interactions have not been included in ice/ocean models hitherto. While it has been discussed in the past, the complexity of doing this has proved insuperable until now. We have provided a potential way to do it, and have given some first predictions of how floe sizes and MIZ width are manipulated by waves in a one-dimensional spectral setting. Most importantly, we have established the machinery to deal with the next stage of development, which is to incorporate two-dimensional interactions arising from a directional sea comprising energy at a comb of different frequencies distributed angularly.

Acknowledgement

References

Ardhuin, F., Rogers, E., Babanin, A.V., Filipot, J.-F., Magne, R., Roland, A., van der Westhuysen, A., Queffeulou, P., Lefevre, J.-M., Aouf, L., Collard, F., 2010. Semiempirical dissipation source functions for ocean waves. Part I: Definition, calibration, and validation. J. Phys. Oceanogr. 40, 1917–1941.

Bennetts, L.G., Squire, V.A., 2012. On the calculation of an attenuation coefficient for transects of ice-covered ocean. Proc. R. Soc. Lond. A 468 (2137), 136–162.

Bretschneider, C.L., 1959. Wave variability and wave spectra for wind-generated gravity waves. Tech. Mem. 118, Beach Erosion Board, U.S. Army Corps Eng.

Drange, H., Simonsen, K., 1996. Formulation of air–sea fluxes in the ESOP2 version of MICOM. Tech. Rep. 125, Nansen Environmental and Remote Sensing Center, Thormhlensgate 47, Bergen 5006, Norway.

Dumont, D., Kohout, A.L., Bertino, L., 2011. A wave-based model for the marginal ice zone including a floe breaking parameterization. J. Geophys. Res. 116 (C04001). http://dx.doi.org/10.1029/2010JC006682.

Feltham, D.L., 2005. Granular flow in the marginal ice zone. Phil. Trans. R. Soc. Lond. A. 363, 1677–1700.

Hasselmann, K., 1962. On the non-linear transfer in a gravity-wave spectrum. Part 1. General Theory. J. Fluid Mech. 12, 481–500.

Hasselmann, K., 1963. On the non-linear transfer in a gravity-wave spectrum. Part 3. Computation of the energy flux and swell-sea interaction for a Neumann spectrum. J. Fluid Mech. 15, 385–398.

Kloster, K., Sandven, S., 2011. Ice motion and ice area flux in the Fram Strait at 79N using ASAR and passive microwave for Feb. 2004–Jul. 2010. Tech. Rep. 322, Nansen Environmental and Remote Sensing Center.

Kohout, A.L., Meylan, M.H., 2008. An elastic plate model for wave attenuation and ice floe breaking in the marginal ice zone. J. Geophys. Res. 113 (C09016), doi:10.1029/2007JC004434.

Masson, D., LeBlond, P.H., 1989. Spectral evolution of wind-generated surface gravity waves in a dispersed ice field. J. Fluid Mech. 202, 111–136.

Meylan, M.H., Masson, D., 2006. A linear Boltzmann equation to model wave scattering in the marginal ice zone. Ocean Modell. 11 (3–4), 417–427.

Ochi, M.K., 1998. Ocean waves. A Stochastic approach. Cambridge University Press.

Roe, P.L., 1986. Characteristic-based schemes for the euler equations. Annu. Rev. Fluid Mech. 18, 337–365.

Sakov, P., Counillon, F., Bertino, L., Liseter, K.A., Oke, P.R., Korablev, A., 2012. TOPAZ4: an ocean-sea ice data assimilation system for the North Atlantic and Arctic. Ocean Sci. 8, 633–656.

Shen, H.H., Hibler, W.D., Leppäranta, M., 1986. On applying granular flow theory to a deforming broken ice field. Acta Mech. 63, 143–160.

Squire, V., Moore, S.C., 1980. Direct measurement of the attenuation of ocean waves by pack ice. Nature 283 (5745), 365–368.

Steele, M., 1992. Sea ice melting and floe geometry in a simple ice-ocean model. J. Geophys. Res. 97 (C11), 17729–17738.

Steele, M., Morison, J.H., Untersteiner, N., 1989. The partition of air-ice-ocean momentum exchange as a function of ice concentration, floe size, and draft. J. Geophys. Res. 94 (C9), 12739–12750.

Strong, C., 2012. Atmospheric influence on Arctic marginal ice zone position and width in the Atlantic sector, February–April 1979–2010. Clim. Dyn. 39 (12), 3091–3102.

Toyota, T., Takatsuji, S., Nakayama, M., 2006. Characteristics of sea ice floe size distribution in the seasonal ice zone. Geophys. Res. Lett. 33 (L02616).

Toyota, T., Haas, C., Tamura, T., 2011. Size distribution and shape properties of relatively small sea–ice floes in the Antarctic marginal ice zone in late winter. Deep-Sea Res. II 58 (9–10), 1182–1193.

Vaughan, G.L., Squire, V.A., 2011. Wave induced fracture probabilities for Arctic sea–ice. Cold Regions Sci. Technol. 67 (1–2), 31–36.

Wadhams, P., Squire, V.A., Goodman, D.J., Cowan, A.M., Moore, S.C., 1988. The attenuation rates of ocean waves in the marginal ice zone. J. Geophys. Res. 93 (C6), 6799–6818.

Widell, K., Østerhus, S., Gammelsrød, T., 2003. Sea ice velocity in the Fram Strait monitored by moored instruments. Geophys. Res. Lett. 30 (L018119).

Williams, T.D., Porter, R., 2009. The effect of submergence on the scattering by the interface between two semi-infinite sheets. J. Fluids Struct. 25, 777–793.

Williams, T.D., Bennetts, L.G., Squire, V.A., Dumont, D., Bertino, L., 2013. Wave–ice interactions in the marginal ice zone. Part 1: Theoretical foundations. Ocean Modell., http://dx.doi.org/10.1016/j.ocemod.2013.05.010.

World Meteorological Organization, 1998. Guide to Wave Forecasting and Analysis, second ed. WMO No. 702. World Meteorological Organization.